Characterization of Three-Dimensional Effects for the Rotating and Parked NREL Phase VI Wind Turbine

Sven Schmitz
Graduate Student Researcher
e-mail: shschmitz@ucdavis.edu

Jean-Jacques Chattot
Professor and Chair
e-mail: jjchattot@ucdavis.edu

Department of Mechanical and Aeronautical Engineering,
University of California,
One Shields Avenue,
Davis, CA 95616-5294

This paper addresses three-dimensional effects which are pertinent to wind turbine aerodynamics. Two computational models were applied to the National Renewable Energy Laboratory Phase VI Rotor under rotating and parked conditions, a vortex line method using a prescribed wake, and a parallelized coupled Navier-Stokes/vortex-panel solver (PCS). The linking of the spanwise distribution of bound circulation between both models enabled the quantification of three-dimensional effects with PCS. For the rotating turbine under fully attached flow conditions, the effects of the vortex sheet dissipation and replacement by a rolled-up vortex on the computed radial force coefficients were investigated. A quantitative analysis of both radial pumping and Coriolis effect, known as the Himmelskamp effect, was performed for viscous as well as inviscid flow. For the parked turbine, both models were applied at various pitch angles corresponding to fully attached as well as stalled flow. For partially stalled flow, computed results revealed a vortical structure trailing from the blade's upper surface close to the 40% radial station. This trailing vortex was documented as a highly unsteady flow structure in an earlier detached eddy simulation by another group, however, it was not directly observed experimentally but only inferred. Computed results show very good agreement with measured wind tunnel data for the PCS model. Finally, a new method for extracting three-dimensional airfoil data is proposed that is particularly well suited for highly stalled flow conditions. [DOI: 10.1115/1.2349548]

Keywords: CFD, Navier-Stokes, vortex method, prescribed wake, coupling, NREL phase VI rotor, three-dimensional effects, three-dimensional polar data

1 Introduction

The Phase VI Unsteady Aerodynamics Experiment (UAE) conducted by the National Renewable Energy Laboratory (NREL) in the NASA Ames (80 ft × 120 ft) Wind Tunnel is an excellent database that provides researchers and modelers with valuable datasets [1,2]. The Blind Comparison study [3] clearly demonstrated that researchers using computational tools still face many challenges in predicting wind turbine aerodynamics. Modelers were surprised by the large scatter among their various predictions of the Phase VI Rotor performance even under the simplest possible case of zero yaw, steady-state, and no-stall conditions [3], corresponding to a wind speed of $U_\infty = 7$ m/s. For this case, rotor power predictions ranged from 25% to 175% of measured with one computational fluid dynamics (CFD) code by Sorensen et al. [4] showing best results. Since then, a number of CFD models have been applied to the Phase VI Rotor; Xu and Sankar [5] and Benjanirat and Sankar [6] applied a hybrid method; Duque et al. [7] performed a full domain Navier-Stokes (NS) analysis; Le Pape and Lecanu [8] used a full domain NS solver and also investigated the effect of the pitch shaft section on local loads; Schmitz and Chattot [9,10] applied a parallelized coupled Navier-Stokes/vortex-panel methodology (PCS) to the Phase VI Rotor at wind speeds surrounding peak power; Langtry et al. [11] recently studied the influence of a transition model within a full domain NS analysis of the Phase VI Rotor. Although the models mentioned above are quite sophisticated and computationally expensive, the predicted power still deviated by 20% from the measured power [3]. Less complex prescribed wake models of Tangler [12], lifting surface prescribed wake code (LSWT), or Chattot [13,14], vortex line method (VLM), showed improved accuracy relative to the computationally expensive codes at a wind speed of $U_\infty = 7$ m/s, however at a much lower computational cost. The question arises as to why wake models can generally predict low-speed rotor performance very well, while sophisticated CFD models still exhibit a significant 20% discrepancy in the predicted power. For a case of fully attached flow along the entire blade, it was found that local blade loads do not significantly depend on the turbulence model used [10]. Furthermore, all CFD models are assumed to have suitable grid spacing at leading and trailing edges in the case of fully attached flow. However, a three-dimensional (3D) grid convergence study or a change in discretization scheme is seldom performed in order to quantify the effect of artificial dissipation on local blade loads.

In general, NS codes suffer from rapid artificial dissipation of vortical structures in the wake. Nevertheless, Fig. 1(*a*) reveals that the experimentally observed trailing vortex sheet is present far downstream. Even an extensive overset grid refinement downstream of the blade performed by Duque et al. [7] with more than 11,000,000 grid points in the NS zone can only convect the trailing vortex sheet for a few revolutions, until it is fully artificially dissipated. In contrast to CFD models, the nature of wake models allows the convection of shed and trailed vorticity far downstream into the wake with very little or no dissipation. The PCS solver [10] combines a near field NS analysis with a prescribed wake model in the far field, and thus we were able to investigate the influence of the vortical wake on results obtained. The comparison

Contributed by the Solar Energy Division of ASME for publication in the JOURNAL OF SOLAR ENERGY ENGINEERING. Manuscript received February 24, 2006; final manuscript received July 16, 2006. Review conducted by Patrick Moriarty. Paper presented at the 25th ASME Wind Energy Symposium/44th AIAA Aerospace Sciences Meeting and Exhibit, Reno, NV, 2006.

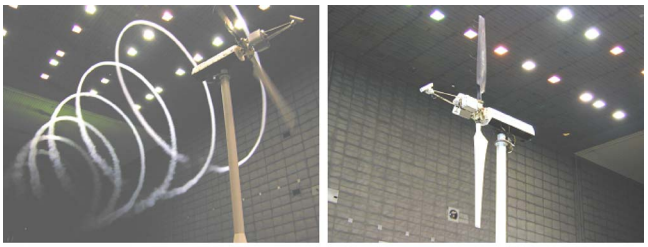

(a) Rotating, Upwind – Sequence S (b) Parked, Upwind – Sequence L

Fig. 1 NREL Phase VI Rotor in the NASA Ames (80 ft×120 ft) wind tunnel (Photographs by L. J. Fingersh, NREL)

of the 3D PCS model with VLM, which uses an uncorrected two-dimensional (2D) polar of the S809 airfoil, enabled the quantification of 3D aerodynamics such as radial pumping and Coriolis effect. It was found that these 3D effects differ for viscous and inviscid flow. Furthermore, the effect of the vortex sheet rollup into a single vortex was investigated with the limiting case of a tip vortex model [5,6].

The parked Phase VI Rotor shown in Fig. 1(*b*) serves as a good test case for the performance prediction of computational models under stalled conditions excluding rotational effects. Recently, Gupta and Leishman [15] used a 2D static stall model based on the Leishman-Beddoes model [16] for the S809 airfoil within a 3D Weissinger-L type of blade model [17] to predict the stall onset and aerodynamic coefficients in the deep stall regime. More accurate results than those of this study [15] were obtained earlier by Johansen and Sorensen [18] who applied their NS code to the parked Phase VI Rotor. They found that a detached-eddy simulation (DES) did not particularly improve the results under stalled conditions. However, their simulations showed considerably more 3D flow structures compared to conventional two-equation Reynolds averaged Navier-stokes (RANS) turbulence models, e.g., k-ω shear stress transport (SST). At one particular pitch angle in the stall regime, they also found a highly unsteady and unstable trailing vortex at the 47% radial station, which only occurred in the DES computations. This vortex was also observed in an accompanying work by Sorensen [19] for the rotating turbine and was attributed to the specific blade design. Schmitz and Chattot [9,10] as well as Tangler [12] recently documented again the possibility of this vortex for the rotating turbine by means of the spanwise distribution of bound circulation. The trailing vortex is due to the complex interaction between local stall and spiral separation. However, it has not been directly observed in the experiments but only inferred. The present paper shows the trailing vortex in a stable form using the PCS model and a conventional two-equation k-ω SST turbulence model by Menter [20]. Furthermore, the effect of the pitch shaft section on local blade loads was analyzed, which to date has only been modeled by Le Pape and Lecanu [8] for the rotating turbine.

The performance predictions of wake models and blade element models (BEM) strongly depend on the polar data used, particularly for stalled flow. In many cases, experimental 2D polars are modified to account for 3D effects. Among the most widely used correction models are those of Snel et al. [21], Du and Selig [22], Chaviaropoulos and Hansen [23], and recently van Rooij and Schepers [24]. The main problem associated with this procedure is that the models are generally tuned to specific airfoils and are therefore not applicable to blade designs equipped with different airfoils. Using CFD codes for the extraction of 3D polar data from a particular blade design and using these data in computationally more efficient wake models or BEMs results in a more efficient design process. However, the extraction of 3D polar data is not straightforward, as local effective angles of attack are initially unknown in a CFD code. Bak et al. [25] and Bjork et al. [26] utilized an *inverse* BEM method based on rotor geometry, wind speed, and force coefficients computed by the CFD code to extract airfoil polars. Unfortunately, the results were not promising and showed deviations even in the linear region of the airfoil data. Sorensen [19] generated a stagnation point location versus angle of attack curve for the S809 airfoil from 2D computations. Using this curve along with the stagnation point location obtained from the 3D pressure distribution, he was able to estimate a corresponding 2D angle of attack. However, the method was questionable when strong 3D effects were present. Furthermore, a set of different stagnation point versus angle of attack curves are required, if the blade is equipped with multiple airfoils. The same method to extract 3D polar data was later used by Le Pape and Lecanu [8] who reported the same difficulties. Recently, Johansen and Sorensen [27] presented a reduced axial velocity method to extract 3D airfoil characteristics from existing CFD computations based on an earlier idea by Hansen et al. [28]. In this method, an average wind speed at the rotor plane from CFD results is used to evaluate the local flow angle. The local angle of attack is then obtained by subtracting the local pitch angle. The present paper proposes a novel approach for extracting 3D airfoil data. This approach is particularly suited for separated and stalled flow conditions.

2 Numerical Methods

Vortex Line Method (VLM). This model [13,14] consists of a lifting line and a rigid wake, which is formed by a helicoidal vortex sheet for the rotating turbine and a plane vortex sheet for the parked turbine. The VLM code uses a cosine distribution of discretization points along the lifting line, which is linked to the infinite series solution of Prandtl's fundamental equation of lifting line theory [29]. The advantage of this method is its convection of trailing vorticity into the wake without dissipation. The rollup of the vortex sheet and increase in stream tube diameter behind the rotor are not accounted for. Both are second order effects with respect to the local induced angle of attack, as the total vorticity content is not changed but only distributed slightly differently. The main ingredients of this method are comprised in Eq. (1).

$$\Gamma(y_j) \Rightarrow \Phi(y_j) \quad \text{Biot-Savart law}$$

$$\alpha(y_j) = \Phi(y_j) - [\pi/2 - \beta(y_j)] \Rightarrow C_l(y_j), C_d(y_j) \quad \text{2D polar data}$$

$$\Gamma(y_j) = -\frac{1}{2} C_l(y_j) \cdot U_\infty(y_j) \cdot c(y_j) \quad \text{Kutta-Joukowski lift theorem} \tag{1}$$

A rigid vortex structure is assumed with a spanwise distribution of bound circulation $\Gamma(y_j)$. The local flow angle $\Phi(y_j)$ at the lifting line is obtained by using the Biot-Savart law. Then, the local effective angle of attack $\alpha(y_j)$ is determined by using the local flow angle $\Phi(y_j)$ and the local blade twist angle $\beta(y_j)$. The local angle of attack $\alpha(y_j)$ is used to find sectional coefficients of lift and drag, C_l and C_d, from a single 2D polar. Finally, the spanwise distribution of bound circulation $\Gamma(y_j)$ is updated using the Kutta-Joukowski lift theorem. This loop is repeated, until $\Gamma(y_j)$ is fully converged.

It should be emphasized that a single 2D polar was used in the VLM code without any 3D correction. The effect of using 3D corrected polar data in VLM code simulations was not examined in this study. Instead, the objective was to illustrate the discrepancies observed between VLM and PCS and thus to characterize 3D effects for the rotating and parked NREL Phase VI Rotor by comparison with measured wind tunnel data. The 2D polars differed for the rotating and parked cases, as the governing flow conditions were essentially different, see Sec. 1. For the rotating case, fully attached viscous and inviscid flow was considered, while for the parked case, blade loads were predicted for condi-

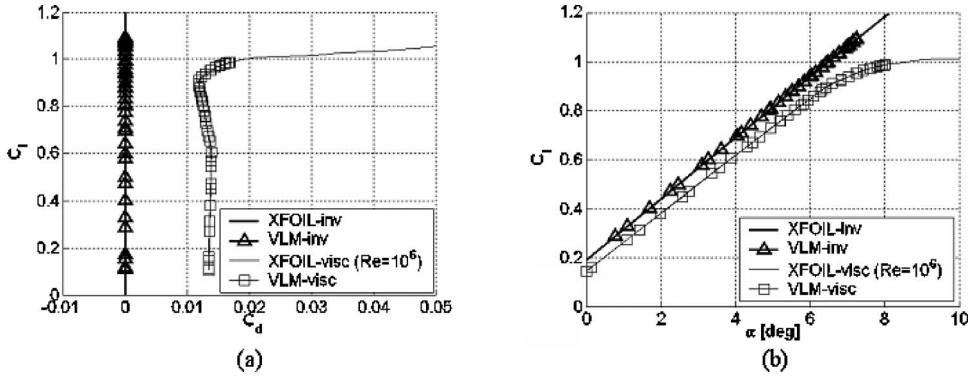

Fig. 2 2D polar data for the S809 airfoil and VLM operating points (NREL Phase VI Rotor, rotating, *S*-sequence, $U_\infty = 7$ m/s)

tions ranging from attached to stalled flow.

"Rotating" NREL Phase VI Turbine (S—Sequence, $U_\infty = 7$ m/s). A total number of 41 discretization points along the lifting line was sufficient to obtain consistent results for fully attached flow. Two-dimensional polars for the S809 airfoil were created with XFOIL [30] for inviscid flow as well as viscous flow at a Reynolds number of $\mathrm{Re} = 10^6$. XFOIL was utilized because of its capability of building an inviscid profile polar. Figure 2 shows the 2D polars including the operating points of the VLM code.

"Parked" NREL Phase VI Turbine (L—Sequence, $U_\infty = 20.1$ m/s). The blade was discretized with 81 points along the lifting line in order to obtain improved resolution of the separated and stalled flow regions, which were not investigated for the rotating turbine. Wind tunnel measurements of the S809 airfoil obtained at Colorado State University (CSU) [31] at a Reynolds number of $\mathrm{Re} = 6.5 * 10^5$ were used as 2D polar data in the VLM code. Figure 3 shows the 2D polar including the operating points of the VLM code for the limits being investigated in this work, i.e., attached flow and stalled flow.

Parallelized Coupled Navier-Stokes/Vortex-Panel Solver (PCS). The objective of the PCS method [9,10] is to combine the advantages of both NS and vortex methods while maintaining computational efficiency. Navier-Stokes analysis is mandatory in the vicinity of the blade in order to capture complex 3D flow phenomena. The vortex method accounts for the far field and ensures that vortical structures are convected downstream of the rotor without dissipation. It is important to emphasize that the relatively small size of the NS zone reduces the computational cost to a fraction of that of a full domain NS analysis. The PCS method uses a commercial NS code CFX 5.7 for the analysis of the near field and the in-house VLM code for the far field.

The spanwise circulation $\Gamma(y_j)$ is distributed along a bound vortex and the change $\delta\Gamma(y_j)$ along the rigid wake; the wake model uses a discrete form of the Biot-Savart law and imposes induced velocities on the outer boundary of the NS zone. The boundary conditions between the NS and wake zones are enforced every ten iterations of the NS solver until full convergence is achieved. The methodology of the coupled solver along with details on its mathematical formulation was described in a previous paper [10]. The spanwise distribution of bound circulation is the main component of the coupling methodology. It is determined by Stokes' theorem at each radial station according to

$$\Gamma(y_j) = \oint_{L_j} v\,ds = \int_{A_j}\int \omega\,dA \tag{2}$$

where the contour line L_j includes all sources of vorticity, namely, the boundary layer and separated flow regions. Figure 4 shows vorticity contours for the parked turbine at the 90% radial station at a pitch angle corresponding to $\alpha_{47} = 33.50$ deg. The upper airfoil surface exhibits leading edge stall, while the flow is fully attached along the lower surface. It can be seen that the far field is essentially inviscid and irrotational. Note that the sectional Reynolds numbers range between $460{,}000 < \mathrm{Re} < 960{,}000$ for the parked turbine. In order for the method to be accurate, the contour line L_j must encompass all the vorticity produced on the airfoil. One restriction to the shape of the contour line L_j is that it has to be orthogonal to the incoming flow direction and pass through the trailing edge, see Fig. 4, as no additional vorticity is produced downstream of the trailing edge. The contour line L_j is closed around the airfoil with a fourth order polynomial. It has a total of

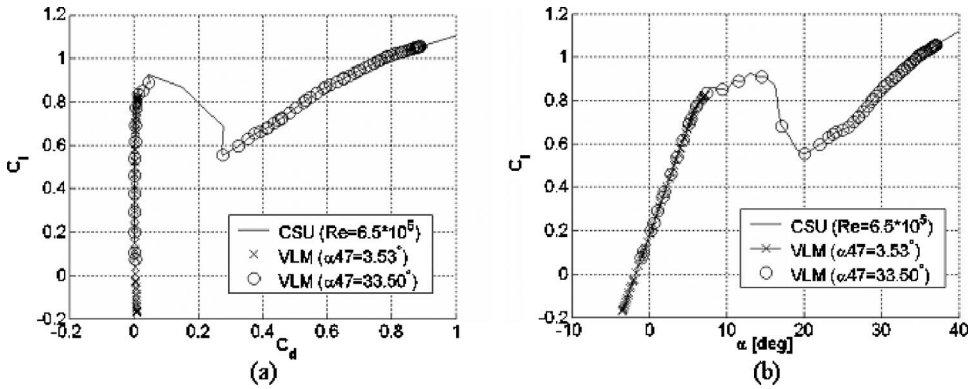

Fig. 3 2D polar data for the S809 airfoil and VLM operating points (NREL Phase VI Rotor, parked, *L*-sequence, $U_\infty = 20.1$ m/s)

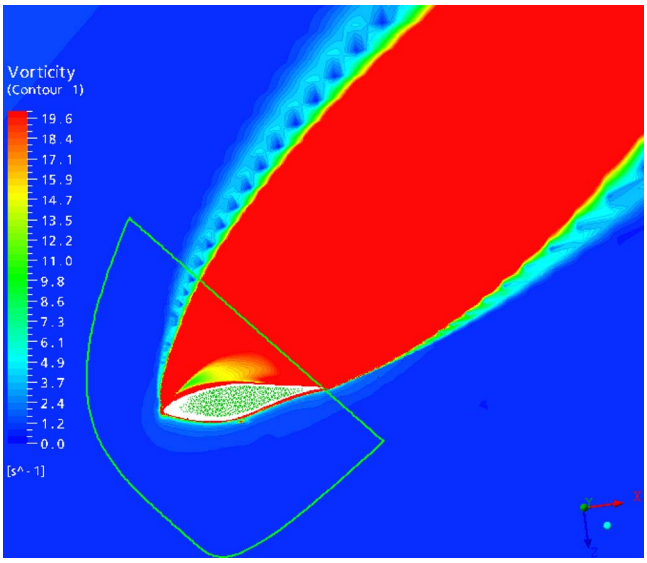

Fig. 4 Vorticity contours and contour line at $r/R=0.90$ (Parked, L-sequence, $U_\infty=20.1$ m/s, $\alpha_{47}=33.50$ deg)

approximately 500 discretization points along its contour in order to ensure an accuracy of $\Gamma(y_j)$ on the order of 10^{-5} m^2/s. Nodal values are interpolated along the contour line L_j. The application of Stokes' theorem in Eq. (2) ensures correct determination of the spanwise bound circulation $\Gamma(y_j)$.

As far as the NS solver is concerned, CFX 5.7 uses a finite-volume higher order discretization technique combined with an algebraic multigrid method. In this work, the flow was assumed to be steady and fully turbulent. The k-ω SST turbulence model by Menter [20] was used for all computations. The rotor blade was meshed with 120 points along its contour, 50 points in the near wake, and 40 points distributed along the blade span with a maximum grid expansion factor of 1.1. A grid independence study was performed for 2D flow [10] around the S809 airfoil and revealed that the normal and chordwise grids are well suited. A similar independence study of the spanwise NS grid was not performed. However, the number of points along the blade span was found to be adequate in the vortex model for calculating induced velocities to an accuracy of 2% of their values [10]. Figures 5 and 6 exhibit some grid details for the rotating and parked turbine. At this stage, the pitch shaft section was not modeled for the rotating case, see Fig. 5(a), but was considered for the parked case. The NS grid in Fig. 5 contains a total of 800,000 nodes, while the grid in Fig. 6 contains a total of 1,300,000 nodes. To distribute the computational load, these grids were partitioned on a cluster of seven processors. A larger domain size was chosen for the parked turbine, as highly stalled flow was investigated. As far as the grid topologies in Figs. 5 and 6 are concerned, C-type meshes were built upon different wake surfaces originating from the blade's trailing edge. For the rotating turbine, the wake surface was

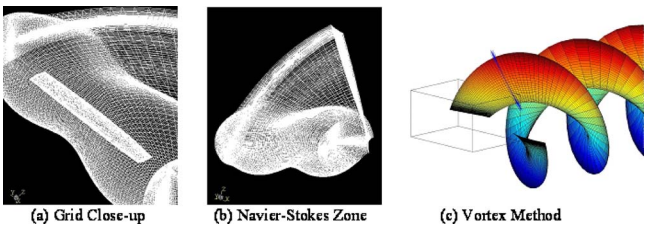

Fig. 5 Decomposition of computational grid into near field and far field, rotating

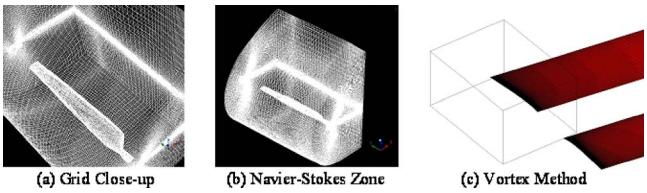

Fig. 6 Decomposition of computational grid into near field and far field, parked

aligned with the first 60 deg of azimuth of the helicoidal vortex sheet created by the vortex model such that vortex filaments in Fig. 5(c) pass between nodes of the NS zone in Fig. 5(b). This complex grid topology ensured that trailing vorticity was captured in the best possible way. For further details, consult Ref. [10]. For the parked turbine, blade pitch angles of up to 30 deg were considered. Figures 5(c) and 6(c) reveal that the second blade was modeled by symmetry in the vortex method. It should be noted that blade-tower interaction was not accounted for in this study.

Near-wall treatment was handled by scalable wall functions. The advantage of the scalable wall function approach is that the surface of the blade coincides with the edge of the viscous sublayer at $y^+=11$. Thus, computed values for the nondimensional wall distance y^+ are not allowed to fall below this limit, which eliminates fine grid inconsistencies of traditional wall functions, see Grotjans and Menter [32]. The CFX-5.7.1 USER MANUAL [33] recommends $20<y^+<100$ using wall functions. Computed values for y^+ stayed below 100 for all cases. The solution converged at a residual of 10^{-6} Pa for the pressure. The NS solver, CFX 5.7, uses an "alternate rotation model" for the advection term of the Coriolis force in the momentum equations. The original advection term is modified to involve the absolute frame velocity instead of the relative frame velocity, which was found to reduce numerical errors. Details on the "alternate rotation model" are given in [33].

Extraction of 3D Polar Data from PCS Results. The normal and tangential force coefficients, $C_N(y_j)$ and $C_T(y_j)$, are determined from the NS code solution through local integration of pressure and shear stresses. Figure 7 illustrates the convention used for sectional airfoil force coefficients of the NREL Phase VI Rotor [1]. The aerodynamic force coefficients, $C_l(y_j)$ and $C_d(y_j)$, are determined by a coordinate transformation

$$C_l = C_N \cdot \cos(\alpha) + C_T \cdot \sin(\alpha) \tag{3a}$$

$$C_d = C_N \cdot \sin(\alpha) - C_T \cdot \cos(\alpha) \tag{3b}$$

assuming the local incidence $\alpha(y_j)$ is known. However, $\alpha(y_j)$ is initially unknown in the fully converged solution of the NS code. To obtain the local incidence angle, the converged spanwise distribution of bound circulation $\Gamma(y_j)$ is first obtained by integrating along closed contour lines such as in Fig. 4, and then the Kutta-Joukowski lift theorem is used to determine the spanwise lift coefficients $C_l(y_j)$ [10]. Note that for a parked turbine, the local free

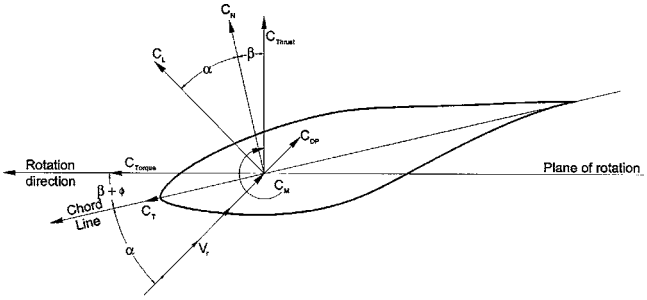

Fig. 7 Sectional airfoil force coefficients (courtesy of NREL)

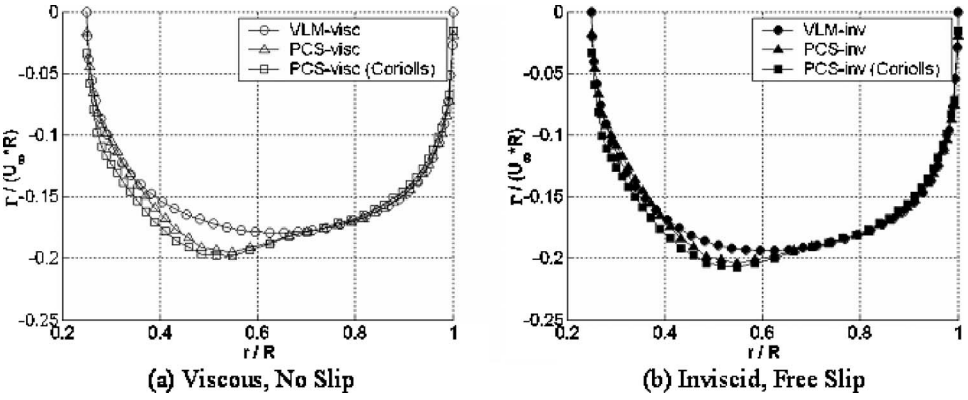

Fig. 8 Distribution of bound circulation (NREL Phase VI Rotor, *S*-sequence, U_∞=7 m/s)

stream wind speed $U_\infty(y_j)$ used in Eq. (1) is equivalent to the wind speed U_∞., while for a rotating turbine, $U_\infty(y_j)$ is obtained from the wind speed and the rotor speed. Using the integrated quantities $C_N(y_j)$ and $C_T(y_j)$, the local angle of attack $\alpha(y_j)$ can then be found by using Eq. (3*a*), and the local drag coefficient $C_d(y_j)$ by using Eq. (3*b*).

At small local incidences $\alpha(y_j)<5$ deg, the drag coefficient $C_d(y_j)$ is two orders of magnitude smaller than the lift coefficient $C_l(y_j)$. Consequently, the drag coefficient $C_d(y_j)$ is very sensitive to any uncertainty in $\alpha(y_j)$, $C_l(y_j)$ and $\Gamma(y_j)$. However, the sensitivity is less for larger incidences in stalled flow, because the relative magnitude of $C_d(y_j)$ increases substantially.

3 Results and Discussion

"Rotating" NREL Phase VI Turbine (*S*-Sequence, U_∞ =7 m/s). Figure 8 shows the spanwise distribution of bound circulation $\Gamma(y_j)$ for VLM and PCS, for viscous as well as inviscid flow, including the Coriolis acceleration within the PCS model. The comparison between VLM and PCS in Fig. 8 illustrates 3D inviscid, 3D boundary layer, and Coriolis effects on the NREL Phase VI Rotor for fully attached flow by means of the spanwise distribution of bound circulation. The fact that VLM uses a pure 2D polar without 3D correction allowed researchers to quantify 3D effects. It can be seen that the magnitude of the circulation $\Gamma(y_j)$ is larger overall for inviscid flow, as friction/pressure drag and lift losses associated with boundary layer displacement are excluded. It is very interesting to note that both computational models predicted similar strengths of root and tip vortices, although the spanwise grid and the mathematical models were different, as described above. Figure 8(*b*) illustrates 3D effects for inviscid flow, observed in differences between VLM-inv and PCS-inv for $0.35<r/R<0.70$. Radial flow acceleration results in a lift benefit for PCS-inv and that cannot be attained with VLM-inv where radial flow was not modeled. Including viscous forces, as in Fig. 8(*a*), results in more pronounced differences between VLM-visc and PCS-visc than for the inviscid case. It is possible that radial forces, or radial pumping, acting on the viscous boundary layer alter the local flow direction more than for inviscid flow, as velocities inside the boundary layer are smaller than the local free stream speed. Again, this is a 3D boundary layer effect that cannot be captured with VLM, because this method is based on strip theory and does not account for spanwise gradients. The Coriolis terms alter the distribution of bound circulation particularly at the blade root, as seen in Fig. 8. Its effect seems to be similar for viscous and inviscid flow on an absolute scale. Radial pumping and Coriolis acceleration combined, known as the Himmelskamp effect [34,35], were studied in many applications. Unlike radial pumping, which is generally directed toward the blade tip, the Coriolis acceleration acts in the chordwise direction. Due to the nature of the radial flow associated with the trailing root vortex on the upper blade surface, the Coriolis force acts toward the trailing edge at the blade root. This was also observed by Du and Selig [36] who studied the Himmelskamp effect on a rotating wind turbine blade using a 3D momentum integral formulation. Thus, the Coriolis force reduces the adverse pressure gradient close to the blade root resulting in a lift benefit on the upper blade surface. At higher wind speeds, the reduction of the adverse pressure gradient delays stall close to the blade root, see again Himmelskamp [34] and Du and Selig [36]. For the NREL Phase VI Rotor and flow conditions in Fig. 8, the radial pumping seems to be more significant than the Coriolis forces, as seen when comparing VLM with PCS. It has to be kept in mind that the Coriolis acceleration is proportional to the angular speed, which equals Ω=72 rpm for the NREL Phase VI Rotor. Therefore, the Coriolis effect is expected to be several orders of magnitude smaller than for a fast rotating propeller such as in Himmelskamp's original experiments [34].

As mentioned in Sec. 1, Navier-Stokes codes dissipate vortical structures in the wake behind rotating lifting bodies after a few revolutions, which is unphysical considering high Reynolds number applications such as wind turbines. The effect of artificial dissipation was simulated in the PCS method by allowing the rigid wake to convect to the far field for either 1 or 20 full revolutions, see also Fig. 5(*c*). Here, 1 revolution is used to model a much larger amount of artificial dissipation than 20 revolutions. Results obtained for the spanwise distribution of bound circulation $\Gamma(y_j)$ can be seen in Fig. 9. Magnitudes for $\Gamma(y_j)$ are higher overall for rapid dissipation of the vortex sheet after 1 revolution. This is attributed to the velocities on the outer boundary of the NS zone in Fig. 5(*b*), which are determined by the wind speed, the rotor speed, and induced velocities of the vortical wake through the

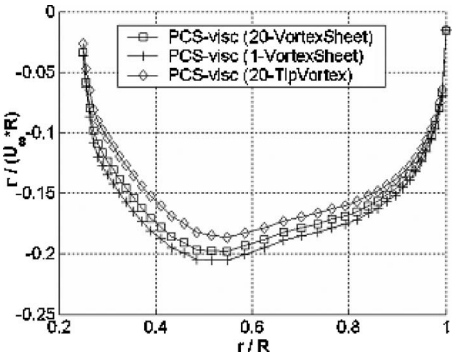

Fig. 9 Effect of vortex sheet dissipation and rollup on bound circulation for 1 and 20 revo modeled in wake (NREL Phase VI Rotor, *S*-sequence, U_∞=7 m/s)

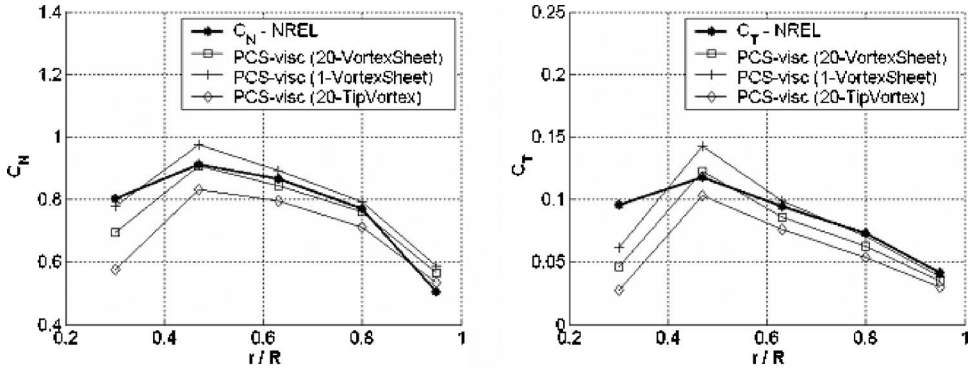

(a) Normal Force Coefficient, C_N (b) Tangential Force Coefficient, C_T

Fig. 10 Normal and tangential force coefficients for 1 and 20 revo modeled in wake (NREL Phase VI Rotor, *S*-sequence, U_∞=7 m/s)

Biot-Savart law. The effect of rapid artificial dissipation can be seen as a lack of vortex sheet induction, which results in higher local angles of attack and bound circulation $\Gamma(y_j)$ in Fig. 9.

As far as the inboard vortex sheet is concerned, its effect was investigated by reducing the entire vortex sheet to one single tip vortex filament, whose strength equals the maximum bound circulation on the blade. This tip vortex model has been applied several times in a hybrid approach by another group [5,6]. In the present case, the tip vortex filament was convected for 20 revolutions into the wake. Results for $\Gamma(y_j)$ are also shown in Fig. 9 and exhibit a distinct underprediction compared to the case of the full vortex sheet, particularly close to the blade root. Spanwise normal and tangential force coefficients in Fig. 10 reveal that the reference case of 20 vortex sheet revolutions performs best in comparison with measured data except for the r/R=0.30 station, which is poorly predicted in all cases. This is attributed to the fact that the actual pitch shaft section of the NREL Phase VI Rotor was not modeled, as seen in Fig. 5(*a*). Values for the measured and computed rotor torque are presented in Table 1. The reference case of 20 vortex sheet revolutions results in a computed rotor torque within 3.5% of the measured value. It is interesting to note that rapid dissipation of the vortex sheet after 1 revolution (1 vortex sheet) overpredicts rotor torque by 8%, while the case of a rolled-up tip vortex filament (20 tip vortex) underpredicts rotor torque by 12% compared to the reference case.

The PCS method presents encouraging results and is believed to be an improved flow physical model through its NS solution of the near wake and the convection of vorticity to the far field without dissipation. Furthermore, the relatively small size of the NS zone makes this method computationally more efficient than a full domain NS analysis. Results revealed that rapid vortex sheet dissipation and roll-up amount to a 20% scatter in computed rotor torque under zero yaw and attached flow conditions.

"Parked" NREL Phase VI Turbine (*L*-Sequence, U_∞ =20.1 m/s). The *L*-sequence was designed to investigate the 3D blade response at static angles of attack in the absence of rotational influences [1]. The rotor was parked with the instrumented blade locked at 0 deg azimuth, see Fig. 1(*b*). All data were collected at zero yaw; the blade pitch was stepped in increments of 5 deg allowing the flow to stabilize around the blade. In the present study, some blade pitch angles were selected ranging from fully attached to almost fully stalled flow. The local blade pitch angle at the 47% radial station α_{47} was chosen as a reference. Computed cases for VLM and PCS are listed in Table 2. The local blade pitch angle was measured with respect to the tunnel center line. Due to blade twist of the NREL Phase VI Rotor [1], local blade pitch angles differed from the reference angle at the 47% radial station.

Results obtained for the normal and tangential force coefficients are shown in Figs. 11 and 12 for PCS and VLM compared to measured NREL data. Both methods show good agreement with NREL data at α_{47}=3.53 deg where the flow was fully attached along the entire blade, see also Fig. 13 comparing PCS computed to measured pressure coefficients. For PCS, the maximum discrepancy between measured and computed values for the normal force coefficient C_N was 0.05 for attached and 0.13 for stalled flow, while the tangential force coefficient C_T deviated from measured data by less than 0.006 for attached and 0.08 for stalled flow. VLM underpredicts normal force coefficients in Fig. 11 at moderate pitch angles and overpredicts at high pitch angles. In Fig. 12, the onset of stall at each radial station is captured fairly well. However, PCS is observed to overpredict tangential force coefficients at the onset of stall as well as in stalled flow, while VLM gives good results in stalled flow at the outboard stations, see Figs. 12(*c*)–12(*e*). It should be recalled that PCS assumed fully turbulent flow. Consequently, the laminar leading edge stall observed at high blade pitch angles in the Phase VI experiment could not be predicted by this method. Figure 14 shows local pressure coefficients at a blade pitch angle of α_{47}=33.50 deg and illustrates the presence of the suction peak in the PCS results at r/R=0.63, 0.80, 0.95. It is this suction peak that is responsible for the overprediction of tangential force coefficients in the stalled flow regime. Furthermore, Fig. 14 reveals that the 47% radial station is not well predicted on the upper blade surface. The measured surface pressure topology shown in Fig. 14(*b*) was analyzed by Schreck and Robinson [37–39] in more detail. It was identified as shear layer impingement where a complex flow region due to laminar leading edge separation reattaches to the suction surface. This complex flow phenomenon could not be attained using the

Table 1 Comparison of measured and computed rotor torque (Nm) for 1 and 20 rev modeled in wake (NREL Phase VI Rotor, *S*-sequence, U_∞=7 m/s)

NREL	PCS visc (20-vortex sheet)	PCS visc (1-vortex sheet)	PCS visc (20-tip vortex)
805.34	775.86	840.04	681.88

Table 2 Blade pitch angles at r/R=0.47 for simulations performed (NREL Phase VI Rotor, *L*-sequence, U_∞=20.1 m/s)

α_{47} (deg)	−1.48	3.53	8.54	13.46	23.49	28.50	33.50
VLM	X	X	X	X	X	X	X
PCS	—	X	—	X	X	—	X

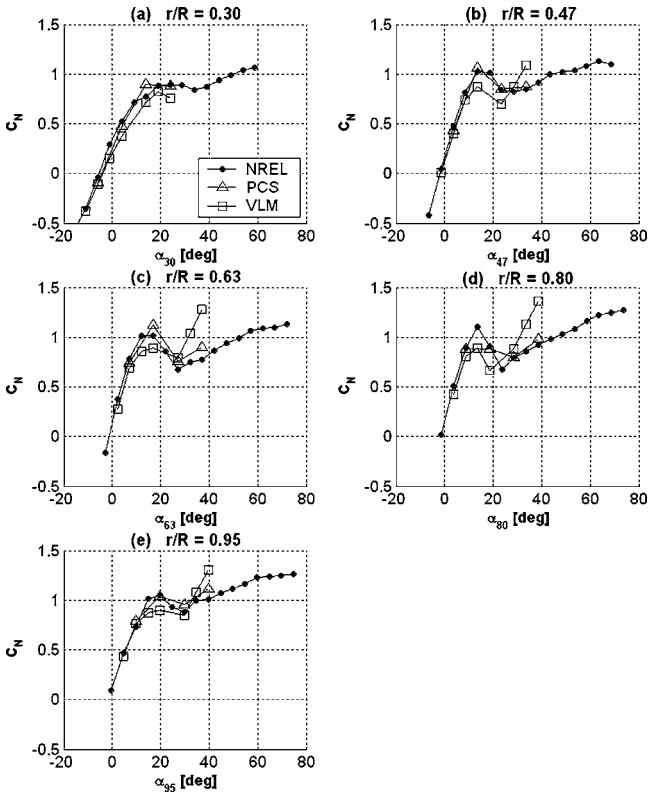

Fig. 11 Normal force coefficient, parked (*L*-sequence, U_∞ =20.1 m/s)

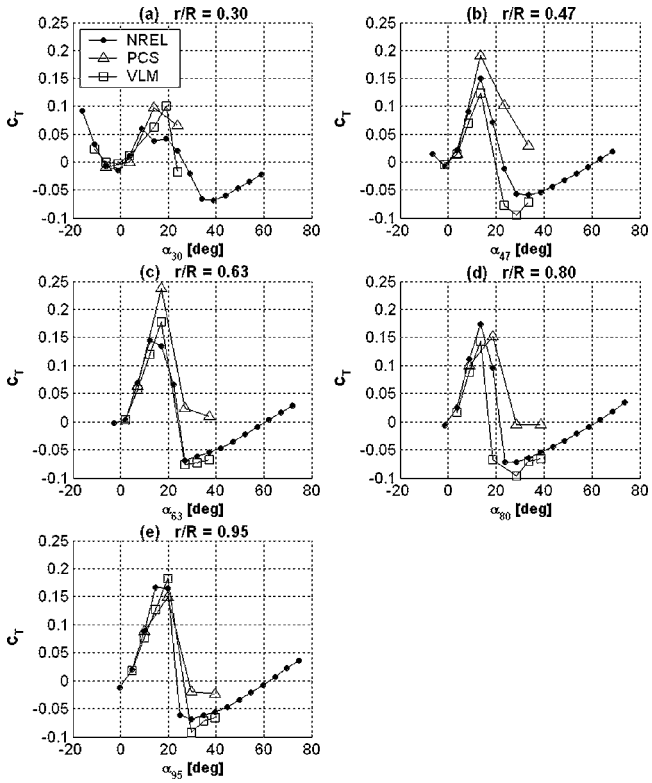

Fig. 12 Tangential force coefficient, parked (*L*-sequence, U_∞ =20.1 m/s)

k-ω SST turbulence model within the PCS method.

Figures 13 and 14 also show the effect of the pitch shaft section on results obtained. For fully attached flow along the entire blade, Fig. 13, it can be seen that PCS results show less agreement with measured data at r/R=0.30, if the pitch shaft section of the NREL Phase VI Rotor was not modeled. For the partially stalled blade, Fig. 14, a distinct difference from not including the root section is again solely found at r/R=0.30. However, the accuracy of the prediction at r/R=0.30 on the upper surface is only mildly influenced by the presence of the pitch shaft section. This is attributed to the neighboring 47% radial station, which was difficult to predict accurately because of the underlying flow separation.

The previous discussion on sectional normal and tangential force coefficients showed the improved aerodynamic load prediction of PCS compared to VLM. The spanwise distribution of bound circulation $\Gamma(y_j)$ is illustrated for both methods in Fig. 15 at various blade pitch angles. Note that PCS did account for the pitch shaft section within its embedded vortex model. Therefore, the bound circulation $\Gamma(y_j)$ starts at the actual blade root of r/R =0.18 as opposed to r/R=0.25 for VLM. Figure 15(*a*) corresponds to fully attached flow. It can be seen that VLM predicts smaller absolute values for $\Gamma(y_j)$ than PCS for most of the blade. This is again attributed to 3D effects, which are less pronounced than for the rotating turbine in Fig. 9. An associated isovorticity surface is shown in Fig. 16(*a*).

Increasing the blade pitch angle to α_{47}=13.46 deg, the curvature in the bound circulation $\Gamma(y_j)$ and gradient $\delta\Gamma(y_j)$ in Fig. 15(*b*) indicate flow separation on the outboard part of the blade between $0.70 < r/R < 0.95$. It is assumed here that any gradient in the spanwise bound circulation $\delta\Gamma(y_j)$ is associated with trailing vorticity. This separated flow region is also illustrated in Fig. 16(*b*) by means of an isovorticity surface. Differences between PCS and VLM are also apparent along the entire blade. The normal force coefficients in Fig. 11 reveal the improved performance prediction of PCS compared to VLM. The very good agreement of PCS results with experimental normal force coefficients in Fig. 11 supports the physical correctness of the 3D bound circulation $\Gamma(y_j)$ determined by Stokes' theorem in Eq. (2).

At α_{47}=23.49 deg in Fig. 15(*c*), small gradients $\delta\Gamma(y_j)$ for

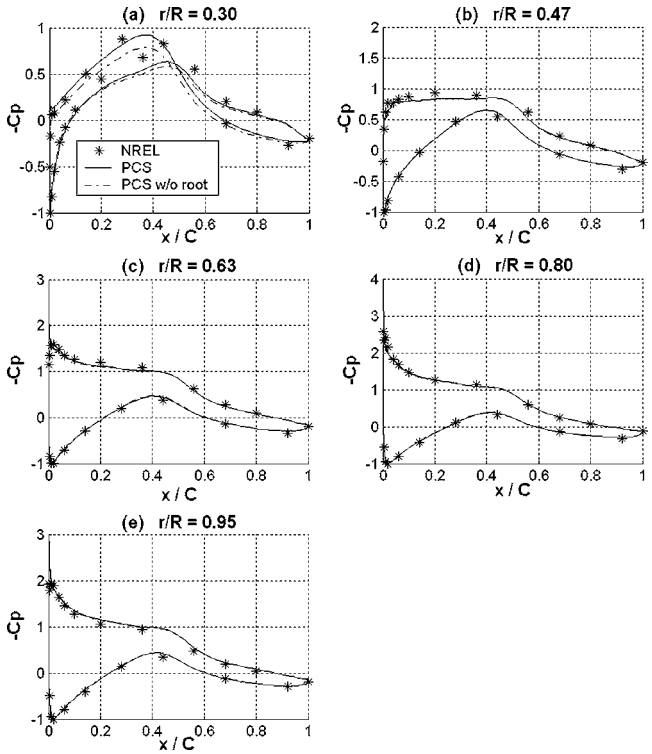

Fig. 13 Pressure coefficient, parked (*L*-sequence, U_∞ =20.1 m/s, α_{47}=3.53 deg)

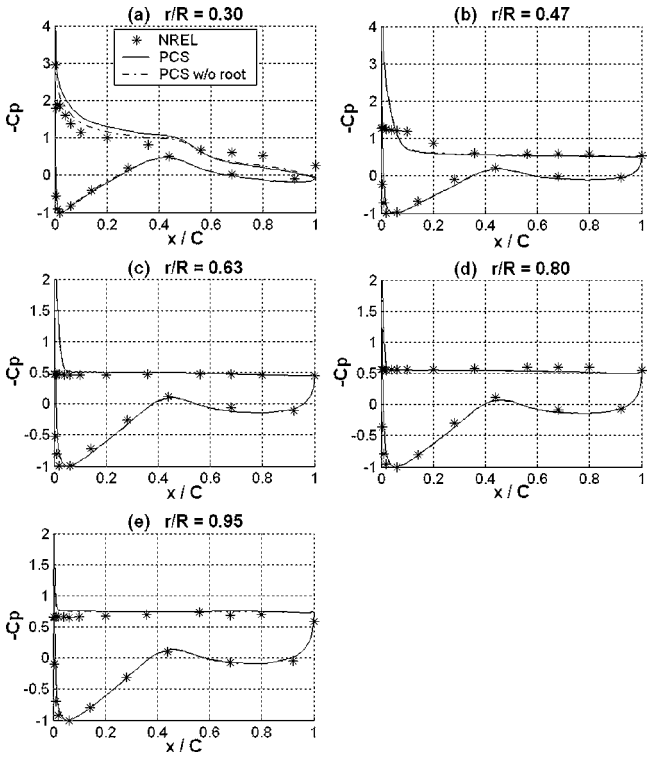

Fig. 14 Pressure coefficient, parked (*L*-sequence, U_∞ =20.1 m/s, α_{47}=23.49 deg)

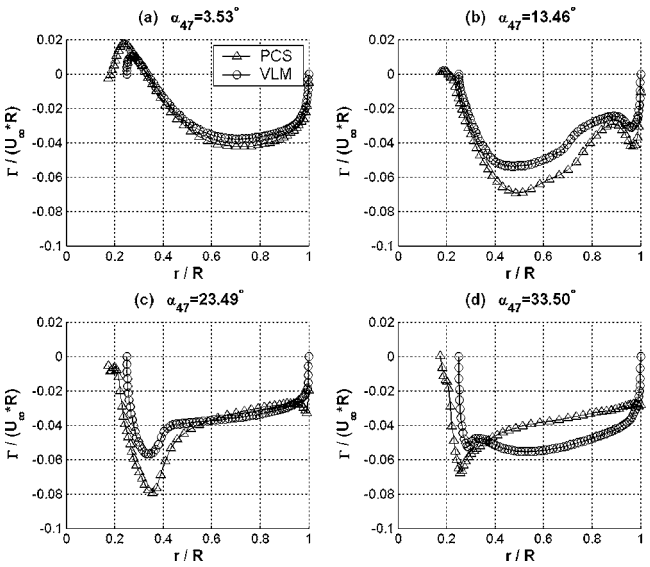

Fig. 15 Distribution of bound circulation, parked (*L*-sequence, U_∞=20.1 m/s)

$r/R>0.50$ provide evidence for the presence of stalled flow in this region. The inboard part of the blade, $r/R<0.35$, is highly loaded in the PCS results. The transition between the inboard and outboard flow regimes is formed by concentrated trailing vorticity about $r/R=0.40$ whose absolute strength $\Delta\Gamma$ is nearly that of the tip vortex. This region of concentrated vorticity can be interpreted as a trailing vortex about $r/R=0.40$ that originates from the blade's upper surface and is counter-rotating to the neighboring root vortex. Its 3D effect can be observed as a downwash inboard of the trailing vortex that results in a stall delay and an upwash outboard of it that enhances stall. This highly 3D flow feature could not be captured with VLM, as this method only matches blade axial and azimuthal flow conditions with 2D data. The PCS predictions of normal force coefficients in Fig. 11 are good for this case. However, some difficulties were observed in the chordwise pressure coefficients in Fig. 14. Figure 16(*c*) illustrates the presence of the trailing vortex in an iso-vorticity surface. The trailing vortex is seen to be stable and attached to the stalled flow regime. This trailing vortex seems to be particular to the NREL Phase VI Rotor, as first postulated by Johansen and Sorensen [18] using DES simulation. There is also evidence of a trailing vortex occurring in the rotating case, as observed by Tangler [12] and Schmitz and Chattot [9,10]. However, the trailing vortex is located more outboard at $r/R=0.47$, which is attributed to rotational effects that further delay the stall inboard and thus shift the vortex to a more outboard position.

A further increase in blade pitch angle to $\alpha_{47}=33.50$ deg, see Fig. 15(*d*), shows that the stalled flow regime progressed inboard for the PCS results. The concentrated vorticity that formed the trailing vortex at a lower blade pitch angle disappeared, see also Fig. 16(*d*). In Fig. 15(*d*), the VLM results for the bound circulation $\Gamma(y_j)$ show a distinct increase in absolute value compared to the lower pitch angle of $\alpha_{47}=23.49$ deg, while the PCS circulation results behave differently. But, as seen in Fig. 11, the PCS computed normal force coefficients C_N show closer agreement with

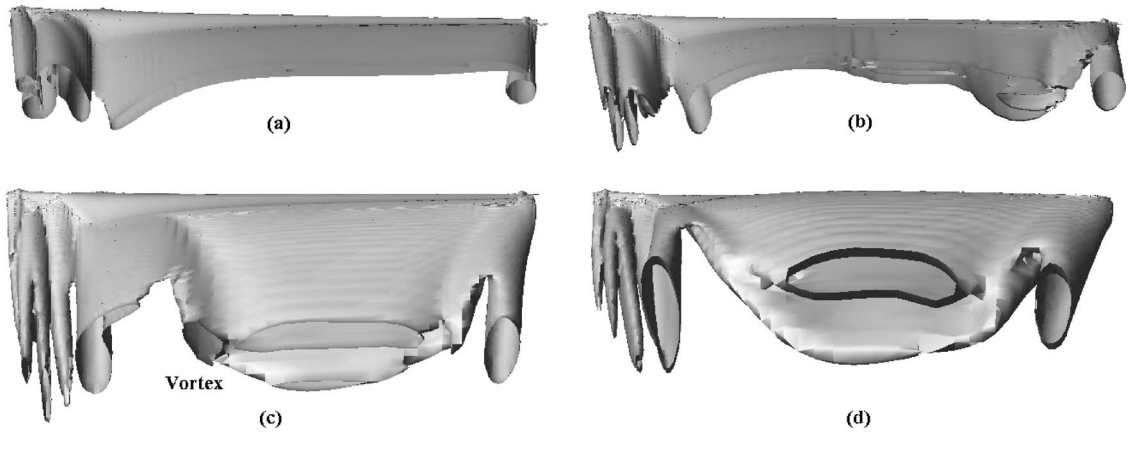

Fig. 16 Iso-vorticity surface behind NREL Phase VI Blade (ω=19 s^{-1}), parked (*L*-sequence, U_∞=20.1 m/s)

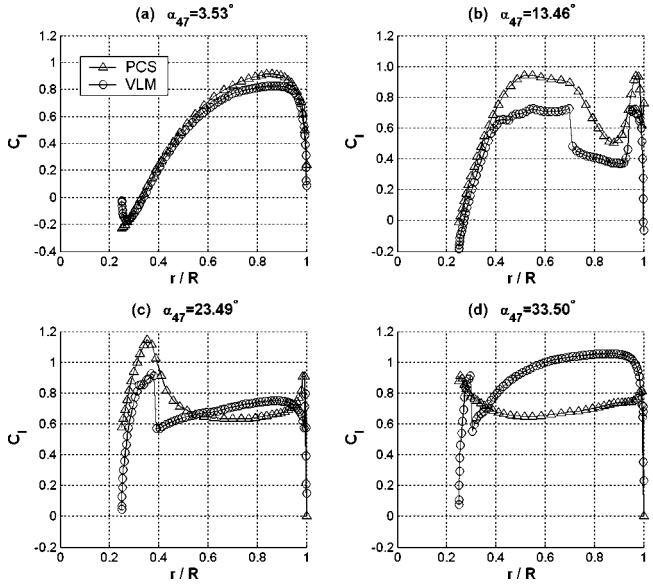

Fig. 17 Spanwise lift coefficient C_l, parked (*L*-sequence, U_∞ =20.1 m/s)

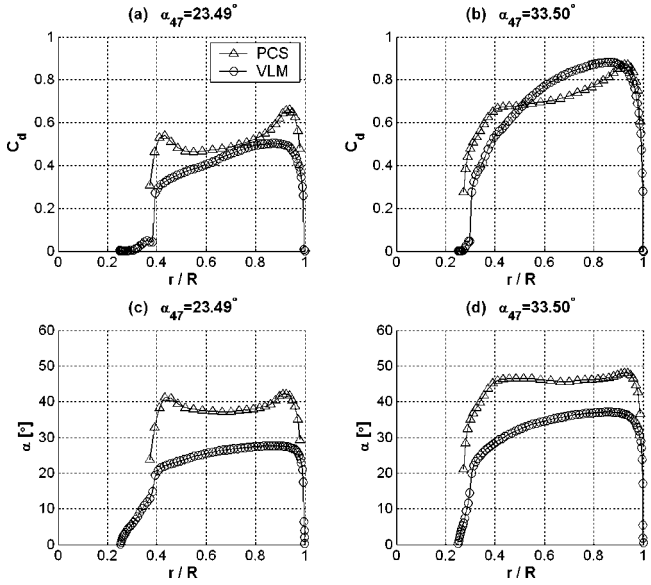

Fig. 18 Spanwise drag coefficient C_d and local incidence α, parked (*L*-sequence, U_∞=20.1 m/s)

NREL data. Given these large differences and agreement with measured data, the advantage of PCS compared to VLM becomes evident when larger separated regions with strong 3D effects are present.

The spanwise lift coefficients $C_l(y_j)$ in Fig. 17 were derived from the Kutta-Joukowski lift theorem for both methods and are proportional to the bound circulation $\Gamma(y_j)$ in Fig. 15. Figures 17(*a*) and 17(*b*) reveal that VLM predicts smaller lift coefficients for moderate blade pitch angles than PCS, however strongly overpredicts lift coefficients for stalled flow in Fig. 17(*d*) at α_{47} =33.50 deg. The fact that PCS shows good agreement with measured data in Fig. 11 supports that this model accurately predicts the bound circulation in Fig. 15 and lift coefficients in Fig. 17. The blade operating points of VLM are shown in Fig. 3 for α_{47} =33.50 deg. It can be seen that VLM mainly operates in the post-stall regime of the experimental CSU S809 polar [30]. The complex 3D flow arising in the post-stall regime cannot be captured with the VLM strip theory approach.

The spanwise drag coefficients $C_d(y_j)$ as well as the local angles of attack $\alpha(y_j)$ are shown in Fig. 18 for the cases with large separated flow regions. For the PCS results, local angles of attack $\alpha(y_j)$ were determined via lift coefficients $C_l(y_j)$ through the extraction method presented in Sec. 2. Only local angles of attack $\alpha(y_j) > 20$ deg were considered, as no consistent results were found for smaller angles due to the uncertainties described in Sec. 2. Values for the drag coefficients $C_d(y_j)$ are shown in Fig. 18(*a*) for α_{47}=23.49 deg. A distinct drag jump can be observed close to the 40% radial station. This jump is associated with the trailing vortex in Fig. 16(*c*), which was also reported by Tangler [12] for the rotating case close to peak power. The difference between VLM and PCS is emphasized in this region due to the 3D character of the flow. The three dimensionality of the flow is even more pronounced for the local angles of attack $\alpha(y_j)$ in Fig. 18(*c*). Here, PCS predicts larger incidences than VLM in the stalled flow regime. Similar behavior is found in Figs. 18(*b*) and 18(*d*) for α_{47}=33.50 deg. It seems that vortex methods such as VLM underpredict the local angles of attack $\alpha(y_j)$ in stalled flow. Note that PCS predicted normal force coefficients C_N show good agreement with experimental data in Fig. 11, while tangential force coefficients C_T are overpredicted in Fig. 12 for large incidences.

4 Conclusions

This work validated a coupled Navier-Stokes/vortex-panel methodology (PCS) against measured data for the NREL Phase VI Rotor under rotating and parked conditions. A comparison between PCS and a vortex line method (VLM), which is based on strip theory and a single 2D polar, enabled the rigorous quantification of 3D effects for the Phase VI Rotor under attached and stalled flow conditions. The effect of radial flow, Coriolis acceleration, vortex sheet reduction to a single vortex, and vortex sheet dissipation was investigated at zero yaw for fully attached flow along the entire blade. It was found that the predicted rotor torque varied by 20%, with the PCS case showing closest agreement with NREL data when including the entire vortex sheet for up to 20 revolutions. The parked Phase VI Rotor was studied for fully attached and stalled flow. The effect of the pitch shaft section on local pressure coefficients was investigated with PCS. Results obtained by PCS showed good agreement with measured data even under highly stalled flow conditions; results obtained by VLM showed good agreement with measured data for fully attached flow. A trailing vortex at the 40% radial station was detected by means of the spanwise distribution of bound circulation. A novel approach was used to extract the local lift and drag coefficients at high angles of attack using the spanwise distribution of bound circulation determined by Stokes' theorem. This method of extracting 3D airfoil characteristics can be applied to any NS solution and any airfoil cross section. It can also be utilized in future investigations of complex 3D wind turbine flow phenomena.

The PCS solver combines the strengths of two methods, the resolution of 3D effects within the near field NS zone and the dissipation-free convection of trailing vorticity to the far field by means of a vortex model. This method is computationally much more efficient than a full domain NS analysis due to the relatively small size of the NS zone.

Acknowledgment

The authors wish to thank Dr. Scott Schreck from NREL for providing the UAE data of the Phase VI Rotor under parked conditions. Computations were made possible on the parallel cluster of Professor Roger Davis at the Department of Mechanical and Aeronautical Engineering, UC Davis.

Nomenclature

A = area, m^2
c = local chord length, m
C_d = drag coefficient
C_l = lift coefficient
C_N = normal force coefficient
C_P = pressure coefficient
C_T = tangential force coefficient
k = turbulent kinetic energy, $kg\ m^2\ s^{-2}$
L = contour line, m
r = local radius, m
R = rotor radius, m
U_∞ = wind speed, $m\ s^{-1}$
$\mathbf{v}$ = velocity vector, $m\ s^{-1}$
y = spanwise Cartesian coordinate, m
y^+ = nondimensional wall distance
α = local angle of attack, deg
α_{47} = blade pitch angle at the 47% radial station, deg
β = blade twist angle, deg
Γ = spanwise circulation, $m^2\ s^{-1}$
$\delta\Gamma$ = local vortex strength, $m^2\ s^{-1}$
Φ = local flow angle, deg
Ω = angular rotor speed, rev/min
ω = vorticity vector, s^{-1}

Abbreviations

BEM = blade element model
CFD = computational fluid dynamics
CSU = Colorado State University
DES = detached eddy simulation
LSWT = lifting surface prescribed wake code
NREL = National Renewable Energy Laboratory
NS = Navier-Stokes
PCS = parallelized coupled solver
RANS = Reynolds averaged Navier-Stokes equations
SST = shear-stress transport
UAE = unsteady aerodynamics experiment
VLM = vortex line method

References

[1] Hand, M. M., Simms, D. A., Fingersh, L. J., Jager, D. W., Cotrell, J. R., Schreck, S., and Larwood, S. M., 2001, "Unsteady Aerodynamics Experiment Phase VI: Wind Tunnel Test Configurations and Available Data Campaigns," NREL/TP-500–29955.

[2] Fingersh, L. J., Simms, D., Hand, M., Jager, D., Cotrell, J., Robinson, M., Schreck, S., and Larwood, S., 2001, "Wind Tunnel Testing of NREL's Unsteady Aerodynamics Experiment," AIAA-2001–0035, pp. 194–200.

[3] Simms, D., Schreck, S., Hand, M., and Fingersh, L. J., 2001, "NREL Unsteady Aerodynamics Experiment in the NASA-Ames Wind Tunnel: A Comparison of Predictions to Measurements," NREL/TP-500–29494.

[4] Sorensen, N. N., Michelsen, J. A., and Schreck, S., 2002, "Navier-Stokes Predictions of the NREL Phase VI Rotor in the NASA Ames 80 ft × 120 ft Wind Tunnel," Wind Energy, **5**(2–3), pp. 151–169.

[5] Xu, G., and Sankar, L., 2002, "Application of a Viscous Flow Methodology to the NREL Phase VI Rotor," AIAA-2002–0030.

[6] Benjanirat, S., and Sankar, L., 2003, "Recent Improvements to a Combined Navier-Stokes/Full-Potential Methodology for Modeling Horizontal Axis Wind Turbines," AIAA-2004-0830.

[7] Duque, E. P. N., Burklund, M. D., and Johnson, W., 2003, "Navier-Stokes and Comprehensive Analysis Performance Predictions of the NREL Phase VI Experiment," Sol. Energy, **125**, pp. 457–467.

[8] Le Pape, A., and Lecanu, J., 2004, "3D Navier-Stokes Computations of a Stall-regulated Wind Turbine," Wind Energy, **7**(4), pp. 309–324.

[9] Schmitz, S., and Chattot, J. J., 2005, "Wind Turbine Blade Aerodynamics of the NREL Phase VI Rotor near Peak Power," AIAA-2005-4850.

[10] Schmitz, S., and Chattot, J. J., 2005, "A Parallelized Coupled Navier-Stokes/Vortex-Panel Solver," Sol. Energy, **127**, pp. 475–487.

[11] Langtry, R. B., Gola, J., and Menter, F. R., 2006, "Predicting 2D Airfoil and 3D Wind Turbine Rotor Performance using a Transition Model for General CFD Codes," AIAA-2006-0395.

[12] Tangler, J., 2004, "Insight into Wind Turbine Stall and Post-stall Aerodynamics," Wind Energy, **7**(3), pp. 247–260.

[13] Chattot, J. J., 2002, "Design and Analysis of Wind Turbines Using Helicoidal Vortex Model," Comput. Fluid Dyn. J., **11**(1), pp. 50–54.

[14] Chattot, J. J., 2004, "Helicoidal Vortex Model for Steady and Unsteady Flows," AIAA-2004-0829; Comput. Fluids, **35**(7), pp. 733–741.

[15] Gupta, S., and Leishman, J. G., 2005, "Stall Modeling of a Parked Wind Turbine Blade and Comparison With Experiment," AIAA-2005-0771.

[16] Leishman, J. G., and Beddoes, T. S., 1995, "A Semi-Empirical Model for Dynamic Stall," J. Am. Helicopter Soc., **117**, pp. 200–204.

[17] Weissinger, J., 1947, "The Lift Distribution of Swept-Back Wings," NACA TM 1120.

[18] Johansen, J., and Sorensen, N. N., 2002, "Detached-Eddy Simulation of Flow around the NREL Phase-VI Blade," AIAA-2002-0032.

[19] Sorensen, N. N., 2000, "Evaluation of 3D effects from 3D CFD computations," IEA Joint Action, *Aerodynamics of Wind Turbines, 14th Symposium*, S. E. Thor, ed., International Energy Agency.

[20] Menter, F. R., 2001, "Zonal Two Equation k-ω Turbulence Models for Aerodynamic Flows," AIAA 2001-0879.

[21] Snel, H., Houwink, B., Bosschers, J., Piers, W. J., van Bussel, G. J. W., and Bruining, A., 1993, "Sectional Prediction of 3-D Effects for Stalled Flow on Rotating Blades and Comparison with Measurements," *Proceedings of the European Wind Energy Conference EWEC93*, A. D. Garrad et al., eds., Bedford, UK, pp. 395–399.

[22] Du, Z., and Selig, M., 1998, "A 3-D Stall-Delay Model for Horizontal Axis Wind Turbine Performance Predictions," AIAA-1998-0021.

[23] Chaviaropoulos, P. K., and Hansen, M. O. L., 2000, "Investigating Three-Dimensional and Rotational Effects on Wind Turbine Blades by Means of a Quasi-3D Navier-Stokes Solver," J. Fluids Eng., **122**, pp. 330–336.

[24] van Rooij, R., and Schepers, J., 2005, "The Effect of Blade Geometry on the Normal Force Distribution of a Rotating Blade," AIAA-2005-0777.

[25] Bak, C., Fuglsang, P., Sorensen, N. N., Madsen, H. A., Shen, W. Z., and Sorensen, J. N., 1999, "Airfoil Characteristics for Wind Turbines," Riso-R-1065-(EN), Riso National Laboratory, Roskilde, Denmark.

[26] Bjork, A., Ronsten, G., and Montgomerie, B., 1995, "Aerodynamic Section Characteristics of a Rotating and Non-rotating 2.375 m Wind Turbine Blade," FFA TN 1995–03, FFA, Bromma, Sweden.

[27] Johansen, J., and Sorensen, N. N., 2004, "Airfoil Characteristics from 3D CFD Rotor Computations," Wind Energy, **7**, pp. 283–294.

[28] Hansen, M. O. L., Sorensen, N. N., Sorensen, J. N., and Michelsen, J. A., 1997, "Extraction of Lift, Drag, and Angle of Attack From Computed 3-D Viscous Flow Around a Rotating Blade," *Proceedings of the European Wind Energy Conference EWEC97*, R. Watson, ed., Slane County Meath, Republic of Ireland: Irish Wind Energy Association, Dublin, pp. 499–502.

[29] Anderson, J. D., Jr., 2001, *Fundamentals of Aerodynamics*, 3rd ed., McGraw-Hill, New York, 2001.

[30] Drela, M., 1989, "XFOIL: An Analysis and Design System for Low Reynolds Number Airfoils," *Low Reynolds Number Aerodynamics*, T. J. Mueller ed., Lecture Notes in Engineering No. 54, Springer-Verlag, Berlin.

[31] Butterfield, C. P., Musial, W. P., and Simms, D. A., 1992, "Combined Experiment Phase I Final Report," NREL/TP-257-4655, Golden, CO.

[32] Grotjans, H., and Menter, F. R., 1998, "Wall Functions for General Application CFD Codes," *ECCOMAS 98 Proceedings of the Fourth European Computational Fluid Dynamics Conference*, John Wiley and Sons, New York, pp. 1112–1117.

[33] *CFX-5.7.1 User Manual*, 2005, "CFX-5 Solver Theory: Basic Solver Capability Theory," CFX ANSYS Inc., Canonsburg PA, p. 32.

[34] Himmelskamp, H., 1950, "Profiluntersuchungen an Einem Umlaufenden Propeller," Diss. Goettingen 1945, Max-Planck-Inst. fuer Stroemungsforschung, Goettingen, Report No. 2.

[35] Schlichting, H., 1979, *Boundary Layer Theory*, McGraw-Hill, New York, pp. 694–696.

[36] Du, Z., and Selig, M. S., 2000, "The Effect of Rotation on the Boundary Layer of a Wind Turbine Blade," Renewable Energy, **20**, pp. 167–181.

[37] Schreck, S., and Robinson, M., 2003, "Boundary Layer State and Flow Field Structure Underlying Rotational Augmentation of Blade Aerodynamic Response," Sol. Energy, **125**, pp. 448–456.

[38] Schreck, S., and Robinson, M., 2004, "Tip Speed Ratio Influences on Rotationally Augmented Boundary Layer Topology and Aerodynamic Force Generation," Sol. Energy, **126**, pp. 1025–1033.

[39] Schreck, S., and Robinson, M., 2005, "Unsteadiness in HAWT Blade Aerodynamic Forces and Flow Field Structures During Rotational Augmentation," AIAA-2005–0776.